Two-dimensional M_2X_2 (M = transition-metal; X = S, Se, Te) family with emerging semiconducting, semimetallic, and magnetic properties

Y. Yekta,[1] H. R. Ramezani,[1] H. Hadipour,[1] A. Khademi,[2] and S. A. Jafari[3,*]
[1]*Department of Physics, University of Guilan, 41335-1914 Rasht, Iran*
[2]*Department of Physics, Sharif University of Technology, Tehran 11155-9161, Iran*
[3]*2nd Institute of Physics C, RWTH Aachen University, 52074 Aachen, Germany*

(Received 21 February 2025; revised 13 September 2025; accepted 9 October 2025; published 31 October 2025)

The exploration for novel two-dimensional (2D) monolayers with diverse electronic characteristics has attracted growing interest in recent years. Using density functional theory (DFT) calculations, we have predicted a new family of 2D transition-metal- (TM) based compounds under the nomenclature M_2X_2 (where M represents TMs and X denotes chalcogen elements like S, Se, and Te). Our investigation delves into the examination of the formation energies, dynamical or thermal stabilities, mechanical properties, electronic structures, and magnetic properties of various systems within this family. Through our computational analyses, we have discovered a total of 35 thermodynamically and dynamically stable M_2X_2 monolayer materials that exhibit remarkable diversity in terms of their electronic and magnetic properties. Our findings will pave the way for the experimental realization of various M_2X_2 structures in the near future. In particular, among the predicted compounds, M_2X_2 (M = Zn, Cd; X = S, Se, Te) are a direct band-gap semiconductor with band gaps between 0.9 to 2.6 eV (1.3 to 3.7 eV) by DFT+Perdew-Burke-Ernzerhof (hybrid functional HSE) calculations. M_2X_2 (M = Ti, Zr, Hf, Tc, Re) are zero-gap semiconductor (semimetals) in standard DFT + PBE calculation. Inclusion of spin-orbit coupling leads to a gap opening of 0.1 eV. Notably, our analysis has also unveiled the magnetic nature of certain materials, such as Mn_2X_2 (X = S, Se), Fe_2X_2 (X = Se, Te), and Ti_2Te_2. The prediction of semiconducting (magnetic) M_2X_2 materials not only offers valuable insights into the underlying electronic properties (magnetism) of 2D systems but also positions these materials as promising candidates for the development of advanced electronic (spintronic) devices.

DOI: 10.1103/c2qq-vc5f

I. INTRODUCTION

Two-dimensional (2D) materials have gained significant attention in recent years due to their unique electronic [1,2], magnetic [3], and optical [4] properties. When these 2D materials host transition-metal (TM) atoms with *d* electrons, they continue to furnish richer physical properties driven by their electronic structures and spin states, as well as the significant spin-orbit coupling (SOC) of the TMs. The interplay between the internal degrees of freedom of electrons, including charge, orbital, and spin holds great potential for both fundamental research and practical device applications. The literature contains numerous examples of TM-based low-dimensional systems, which have been or may potentially be exfoliated in experimental studies. Some important examples of these 2D materials are TM dichalcogenides (TMDs) [5–7] like MoS_2, MXenes [8,9] such as Mo_2C, TM halides [10] such as CrI_3, and newly synthesized MA_2Z_4 family (M = elements of TM; A = Si, Ge; Z = N, P, As) [11–13].

In this paper we use density functional theory (DFT) calculations to predict new 2D TM-based family M_2X_2 (M = TM; X = S, Se, Te). The side and top view crystal structure of the monolayers M_2X_2 are depicted in Figs. 1(a) and 1(b). These materials can be viewed as a AB stacking of two honeycomb MX layers. In AB stacking, the layers are arranged such that one layer is directly on top of the other, with the B atoms of the second layer sitting directly on top of the A atoms of the first layer. Each MX layer has a structure similar to graphene but consists of alternating M (sublattice A) and X (sublattice B) atoms arranged in a buckled hexagonal lattice. We find 35, thermodynamically and dynamically, stable M_2X_2 monolayer materials, which exhibit diverse electronic and magnetic properties. Therefore some of the M_2X_2 materials are expected to be realized in the experiment. Our first-principles calculations indicate that the most stable M_2X_2 systems are metallic. The states around the Fermi energy (E_F) of these compounds are primarily dominated by the *d* orbitals of the TM. Among the predicted compounds, M_2X_2 (where M = Zn, Cd and X = S, Se, Te) are identified as direct band-gap semiconductors, exhibiting band gaps E_g ranging from 0.9 to 2.6 eV as determined by Perdew-Burke-Ernzerhof (PBE) [14] calculations. In contrast, the compounds M_2X_2 (with M = Ti, Zr, Hf, Tc, Re) behave as zero-gap semiconductors or semimetals when

*Contact author: akbar.jafari@rwth-aachen.de

Published by the American Physical Society under the terms of the Creative Commons Attribution 4.0 International license. Further distribution of this work must maintain attribution to the author(s) and the published article's title, journal citation, and DOI.

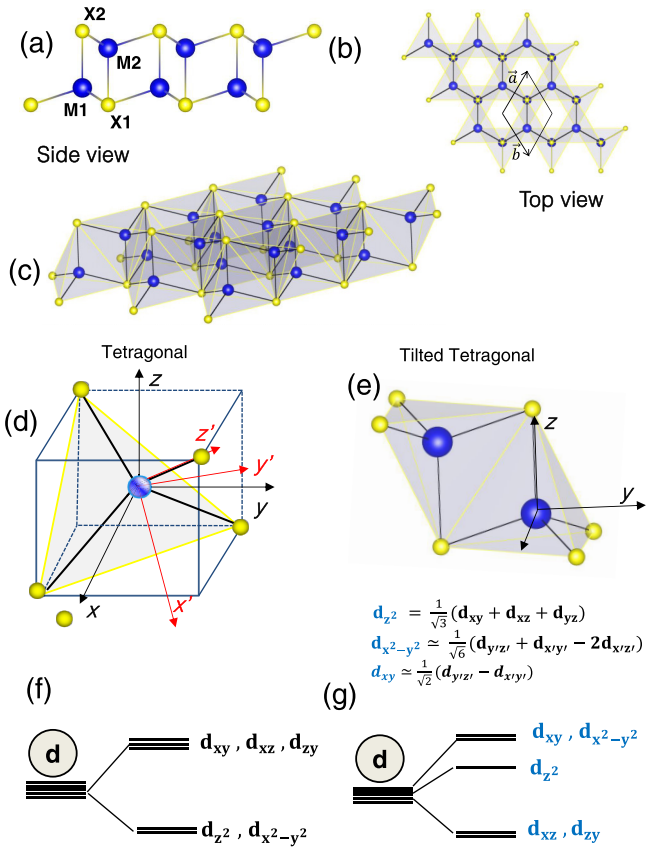


FIG. 1. (a) Side view and (b) top view of the single layer crystal of M_2X_2. (c) Presentation of tetrahedrons in side view crystal structure. (d) One TM bonded with four X atoms in conventional tetrahedral coordination. (e) Tilted tetrahedral coordination of one TM and four chalcogen X atoms. The blue and yellow spheres denote M and X atoms, respectively. Crystal field splitting of d orbitals in (f) conventional tetrahedral structure and (g) tilted tetrahedral structure.

analyzed using standard DFT + PBE calculations. However, the inclusion of SOC modifies their band structure, resulting in the opening of a band gap of approximately 0.1 eV. This broad range of band gaps suggests a potential for diverse applications in optoelectronic devices, particularly in areas requiring tunable electronic properties. Further, the calculation is continued using the computationally more expensive functional of Heyd-Scuseria-Ernzerhof (HSE) [15] to improve the electronic band structures. Overall, the findings highlight rich electronic landscape of these materials and their potential for innovative applications in various fields, including photovoltaics, thermoelectrics, and quantum computing.

Due to the the weak covalent bonding between the TM and the X element in M_2X_2, the number of magnetic systems in the M_2X_2 family is more than in other 2D TM-based families. In fact, the number of magnetic systems in 2D systems are quite scarce. Experimental observations have identified only a few 2D materials, such as CrX_3 (X = Br, I) [16], $Cr_2Ge_2Te_6$ [17], and MX_2 (M = V, Mn; X = Se, Te) [18,19] exhibiting magnetic ordering. Among stable M_2X_2 materials, there are two antiferromagnetic Mn_2X_2 (X = S, Se) systems, and three ferromagnetic systems, namely Fe_2X_2 (X = Se, Te) and Ti_2Se_2. The possibility of magnetic states in M_2X_2 materials not only provides valuable insights into the underlying magnetism of 2D systems but also qualifies these materials as promising candidates for the development of advanced spintronic devices. By exploring the properties and potential applications of the present new family of materials, one can hope to deepen comprehension of magnetism at the nanoscale and unlock new possibilities for innovative technologies.

The rest of the paper is organized as follows. The computational method and crystal structure are presented in Sec. II. Section III focuses on the results and discussion, providing a detailed analysis of the dynamical or thermal stability, electronic structure, and magnetic properties of M_2X_2 monolayers. Finally, in Sec. IV, the paper is summarized.

II. COMPUTATIONAL METHOD AND CRYSTAL STRUCTURE

We consider 2D systems with the chemical formula M_2X_2. Here M represents TM elements and X are chalcogen elements, namely S, Se, and Te. The side and top view crystal structure of the monolayers M_2X_2 are depicted in Figs. 1(a) and 1(b). The optimized structural parameters including in-plane lattice constant ($a = b$), bond lengths between M-X ($d_{M\text{-}X}$), and the z component of the atomic positions are given in Table I. These materials with P-3m1 space group can be considered as an AB stacking of two honeycomb MX layers. In this arrangement, one layer is positioned directly above the other, with the B atoms of the second layer aligned directly over the A atoms of the first layer and vice vesa. Each MX layer has a structure akin to graphene, featuring alternating M (sublattice A) and X (sublattice B) atoms organized in a buckled hexagonal lattice.

In a M_2X_2 structure, the central TM atom is surrounded by four ligands X arranged at the corners of a tetrahedron as shown in the Figs. 1(c). This is completely different from other well-known TM-based compounds like TMDs and MXenes in which, the TM atoms are each bound to six halogen atoms in octahedral or trigonal prismatic coordination [6,8]. Selecting every other vertex of a cube, such that any pair is joined by a diagonal of the cube's face, results in a standard tetrahedron [see Fig. 1(d)]. The three M-X bonds in an M_2X_2 unit form such a configuration, with their ligand ends defining the corners of one face of this tetrahedron. As depicted in Fig. 1(d), in conventional tetrahedral structure, threefold rotation axes is in the $z' = \frac{1}{\sqrt{3}}(i + j + k)$ direction. Other two axis x' and y' are located in a plane constructed by three X atoms.

Here in M_2X_2, the tetrahedron is not like the conventional perovskite tetrahedral structure. The tetrahedron is tilted with respect to the standard Cartesian coordinate x, y, z, in such a way that the threefold rotation axes is in the z direction. As shown in Fig. 1(e), in fact, one of the four triangular sides of tetrahedron is lying on the floor to which the z axis is perpendicular.

Two coordinates are connected to each other by matrix:

$$\begin{pmatrix} \frac{1}{\sqrt{6}} & \frac{1}{\sqrt{2}} & \frac{1}{\sqrt{3}} \\ \frac{1}{\sqrt{6}} & -\frac{1}{\sqrt{2}} & \frac{1}{\sqrt{3}} \\ -\frac{2}{\sqrt{6}} & 0 & \frac{1}{\sqrt{3}} \end{pmatrix}. \quad (1)$$

TABLE I. Structural and electronic properties of 60 M_2X_2 candidates. a is the in-plane lattice constant. The x and y coordinates of the atomic positions in the order of M1, M2, X1, and X2 are (1/3, 2/3), (2/3, 1/3), (1/3, 2/3), and (2/3, 1/3) respectively in fractional coordinates. z_{M1}, z_{M2}, z_{X1}, and z_{X2} are the z component of the atomic positions. Bond lengths are given by $d_{M\text{-}X}$. E_g denote band gap calculated by PBE, PBE+SOC, and HSE06+SOC calculations, respectively. E_f is formation energy.

No.	M_2X_2	a (Å)[a]	z_{M1}(Å)	z_{M2}(Å)	z_{X1}(Å)	z_{X2}(Å)	$d_{M1\text{-}X1}$ (Å)[b]	$d_{M1\text{-}X2}$ (Å)[c]	Ground state	$E_g^{PBE}\|E_g^{SOC}\|E_g^{HSE06}$	E_f(eV/atom)
1	Ti_2S_2	3.92	10.30	8.56	7.82	11.04	2.48	2.38	Semiconductor	0.01 | 0.01 | 0.99	−1.19
2	V_2S_2	3.68	10.16	8.70	7.78	11.08	2.38	2.32	Metal		−0.83
3	Cr_2S_2	3.57	10.04	8.81	7.78	11.07	2.26	2.30	Magnetic-Metal		−0.44
4	Mn_2S_2	3.58	10.02	8.84	7.89	10.97	2.13	2.27	Magnetic-Metal	0.00 | 0.00 | 0.81	−0.48
5	Fe_2S_2	3.56	10.20	8.65	8.03	10.82	2.17	2.15	Metal		−0.42
6	Co_2S_2	3.57	10.20	8.65	8.02	10.83	2.18	2.15	Metal		−0.46
7	Ni_2S_2	3.61	10.19	8.67	7.94	10.92	2,21	2.25	Metal		−0.34
8	Cu_2S_2	3.79	10.33	8.52	7.96	10.89	2.37	2.26	Metal		−0.12
9	Zn_2S_2	3.92	10.45	8.41	7.87	10.99	2.33	2.58	Semiconductor	2.62 | 2.56 | 3.77	−0.75
10	Zr_2S_2	4.20	10.39	8.47	7.76	11.10	2.63	2.53	Semiconductor	0.02 | 0.11 | 0.49	−1.28
11	Nb_2S_2	3.96	10.23	8.62	7.70	11.16	2.54	2.46	Metal		−0.78
12	Mo_2S_2	3.86	10.09	8.77	7.69	11.16	2.40	2.48	Magnetic-Metal		−0.28
13	Tc_2S_2	3.87	10.03	8.83	7.78	11.07	2.25	2.46	Semimetal	0.00 | 0.00 | 0.63	−0.25
14	Ru_2S_2	3.80	10.28	8.58	7.96	10.90	2.32	2.28	Metal		−0.18
15	Cd_2S_2	4.31	10.62	8.23	7.81	11.05	2.53	2.81	Semiconductor	1.81 | 1.79 | 2.70	−0.59
16	Hf_2S_2	4.13	10.37	8.49	7.78	11.08	2.59	2.49	Semiconductor	0.01 | 0.10 | 0.54	−0.98
17	Ta_2S_2	3.93	10.23	8.63	7.69	11.17	2.54	2.45	Metal		−0.56
18	W_2S_2	3.88	10.05	8.80	7.64	11.21	2.41	2.52	Metal		−0.04
19	Re_2S_2	3.88	10.00	8.86	7.71	11.15	2.29	2.52	Semimetal	0.02 | 0.00 | 1.06	0.07
20	Ir_2S_2	3.28	10.50	8.36	7.10	11.75	2.27	3.39	Semiconductor	0.03 | 0.07 | 0.22	−0.27
21	Ti_2Se_2	4.05	10.28	8.57	7.65	11.21	2.63	2.51	Semiconductor	0.01 | 0.04 | 0.96	−0.99
22	V_2Se_2	3.79	10.13	8.72	7.61	11.25	2.52	2.45	Metal		−0.58
23	Cr_2Se_2	3.65	9.98	8.87	7.59	11.27	2.40	2.47	Magnetic-Metal		−0.26
24	Mn_2Se_2	3.66	9.97	8.89	7.69	11.17	2.28	2.43	Magnetic-Metal	0.00 | 0.00 | 0.68	−0.41
25	Fe_2Se_2	3.73	10.15	8.70	7.86	10.99	2.29	2.31	Magnetic-Metal		−0.21
26	Co_2Se_2	3.74	10.19	8.66	7.89	10.97	2.31	2.29	Metal		−0.26
27	Ni_2Se_2	3.74	10.16	8.69	7.80	11.06	2.33	2.37	Metal		−0.27
28	Cu_2Se_2	3.76	10.15	8.71	7.64	11.21	2.50	2.42	Metal		−0.11
29	Zn_2Se_2	4.08	10.38	8.48	7.72	11.14	2.47	2.66	Semiconductor	1.83 | 1.62 | 2.63	−0.68
30	Zr_2Se_2	4.33	10.37	8.48	7.59	11.26	2.78	2.66	Semiconductor	0.00 | 0.05 | 0.62	−1.04
31	Nb_2Se_2	4.06	10.21	8.65	7.53	11.33	2.68	2.60	Metal		−0.53
32	Mo_2Se_2	3.94	10.04	8.81	7.50	11.35	2.54	2.63	Metal		−0.17
33	Tc_2Se_2	3.93	10.00	8.86	7.59	11.26	2.40	2.60	Semimetal	0.01 | 0.00 | 0.82	−0.14
34	Ru_2Se_2	3.97	10.23	8.63	7.81	11.05	2.42	2.43	Metal		−0.05
35	Cd_2Se_2	4.45	10.53	8.33	7.63	11.22	2.66	2.89	Semiconductor	1.54 | 1.40 | 2.19	−0.59
36	Hf_2Se_2	4.26	10.35	8.51	7.60	11.26	2.75	2.62	Semiconductor	0.02 | 0.04 | 0.55	−0.75
37	Ta_2Se_2	4.03	10.20	8.65	7.51	11.35	2.70	2.59	Metal		−0.33
38	W_2Se_2	3.95	10.02	8.83	7.46	11.40	2.57	2.66	Metal		0.07
39	Re_2Se_2	3.93	9.97	8.88	7.51	11.35	2.46	2.65	Semimetal		0.16
40	Ir_2Se_2	3.41	10.43	8.42	7.04	11.82	2.40	3.39	Semiconductor	0.03 | 0.08 | 0.16	−0.08
41	Ti_2Te_2	4.27	10.27	8.59	7.43	11.42	2.84	2.72	Magnetic-Metal		−0.48
42	V_2Te_2	3.97	10.11	8.75	7.40	11.46	2.71	2.66	Metal		−0.15
43	Cr_2Te_2	3.79	9.95	8.91	7.37	11.48	2.58	2.67	Magnetic-Metal		0.09
44	Mn_2Te_2	3.74	9.94	8.92	7.43	11.43	2.51	2.62	Magnetic-Metal		0.02
45	Fe_2Te_2	3.62	9.98	8.87	7.39	11.47	2.59	2.56	Magnetic-Metal		0.04
46	Co_2Te_2	3.96	10.19	8.66	7.73	11.13	2.46	2.47	Metal		−0.07
47	Ni_2Te_2	3.89	10.14	8.72	7.62	11.24	2.50	2.52	Metal		−0.20
48	Cu_2Te_2	3.90	10.09	8.77	7.45	11.40	2.63	2.61	Metal		−0.08
49	Zn_2Te_2	4.33	10.36	8.49	7.55	11.31	2.67	2.81	Semiconductor	0.91 | 0.54 | 1.29	−0.47
50	Zr_2Te_2	4.54	10.36	8.50	7.37	11.48	2.98	2.85	Semiconductor	0.01 | 0.03 | 0.55	−0.59
51	Nb_2Te_2	4.22	10.19	8.67	7.31	11.54	2.87	2.79	Metal		−0.18
52	Mo_2Te_2	4.06	10.01	8.84	7.29	11.56	2.72	2.81	Metal		0.09
53	Ru_2Te_2	4.13	10.21	8.65	7.62	11.24	2.59	2.60	Metal		0.11
54	Tc_2Te_2	4.04	9.99	8.86	7.40	11.45	2.59	2.75	Metal		0.05
55	Cd_2Te_2	4.67	10.48	8.38	7.43	11.42	2.86	3.04	Semiconductor	1.02 | 0.63 | 1.33	−0.44

TABLE I. (*Continued*.)

No.	M_2X_2	a (Å)[a]	z_{M1}(Å)	z_{M2}(Å)	z_{X1}(Å)	z_{X2}(Å)	$d_{M1\text{-}X1}$ (Å)[b]	$d_{M1\text{-}X2}$ (Å)[c]	Ground state	$E_g^{PBE}\|E_g^{SOC}\|E_g^{HSE06}$	E_f(eV/atom)
56	Hf_2Te_2	4.38	10.33	8.53	7.27	11.59	3.06	2.82	Magnetic-Metal		−0.29
57	Ta_2Te_2	4.19	10.18	8.68	7.30	11.56	2.88	2.78	Metal		0.03
58	W_2Te_2	4.06	10.00	8.85	7.25	11.61	2.76	2.84	Metal		0.31
59	Re_2Te_2	3.94	9.97	8.89	7.23	11.63	2.74	2.81	Metal		0.29
60	Ir_2Te_2	4.16	10.28	8.58	7.64	11.22	2.58	2.64	Metal		0.04

[a] $a = b$.
[b] $d_{M1\text{-}X1} = d_{M2\text{-}X2}$.
[c] $d_{M1\text{-}X2} = d_{M2\text{-}X1}$.

The effect of this tilting on the configuration of electrons in the present structure is discussed in detail in the following. In standard tetrahedral structure, crystal field splits d orbitals into the same t_{2g} and e_g sets of orbitals as the two orbitals in the e_g set are lower in energy than the three orbitals in the t_{2g} set [see Fig. 1(f)]. For example, the orbital orientation in d_{z^2} state reduces the energy due to weak overlapping of d states with X atoms and weaker Coulomb interaction. The situation is different in the tilted tetrahedral structure. The tetrahedron is tilted in such a way that d_{z^2} orbital has strong overlap with X atoms. Therefore, as depicted in Fig. 1(g), the d_{z^2} orbitals will be a part of high-energy levels. In fact, if we linearly combine the local t_{2g} orbitals as $\frac{1}{\sqrt{3}}(d_{x'y'} + d_{y'z'} + d_{x'z'})$, then we obtain a d_{z^2} orbital oriented perpendicular to the layer. The next two higher-energy orbitals are constructed as other combination of t_{2g} states, namely $d_{x^2-y^2} \simeq \frac{1}{\sqrt{2}}(d_{y'z'} - d_{x'y'})$ and $d_{xy} \simeq \frac{1}{\sqrt{6}}(d_{y'z'} + d_{x'y'} - 2d_{x'z'})$. Note that the higher-energy bands are not of pure t_{2g} character but exhibit admixture of e_g states. The described denominations refer to their dominant orbital character. d_{xz} and d_{yz} are farther from the ligands than the others and therefore experiences less repulsion.

We have carried out the DFT-based calculations for the M_2X_2 compounds using projector augmented wave [20] pseudopotentials, as implemented in the Vienna ab initio simulation package (VASP) [21] within the generalized gradient approximation in PBE parametrization [14]. In addition, the Heyd–Scuseria-Ernzerhorf (HSE06) [15,22] functional is used to correct the underestimated band gaps. The HSE06 functional is applied by mixing 25% of the exact Hartree-Fock exchange potential with 75% of PBE exchange and 100% of PBE correlation energy. The k-point mesh and the cut-off energies are determined by optimization of total energy to converge energy to 10^{-8} eV/unit cell. Therefore, the uniform k-grids of $14 \times 14 \times 1$ in the first Brillouin zone is utilized for the self-consistent field calculation. The optimized kinetic energy cut-off for the wave functions is 450 eV for non-SOC and SOC and 550 eV for HSE+SOC calculations. A vacuum layer of 20 Å is inserted along the nonperiodic direction to prevent the unrealistic interactions between the neighboring layers. For each system, the Broyden-Fletcher-Goldfarb-Shanno quasinewton algorithm is used to relax the internal parameters for the M and X positions to reach sufficiently small forces, as small as 10^{-4} eV/Å. Phonon calculations are carried out employing the finite displacement method 3×3 supercell framework, utilizing the VASP-PHONOPY interface. Atomic displacements of 0.01 Å are applied to perturb the equilibrium atomic positions, and the resulting forces are computed via DFT + PBE. Phonopy postprocessed the VASP-derived force sets to construct the dynamical matrix, enabling precise determination of phonon dispersion relations across high-symmetry paths in the Brillouin zone. *Ab initio* molecular dynamics (AIMD) simulations are carried out using the Nosé-Hoover thermostat to control the system temperature within a canonical NVT ensemble. A $4 \times 4 \times 1$ supercell is employed here with a time step of 3.0 fs and a total simulation time of 6500 fs (6.5 ps). The second-order elastic constants (C_{ij}) are calculated using the stress-strain method with the PBE-GGA approximation. A $16 \times 16 \times 1$ Monkhorst-Pack k-point grid and a plane-wave cutoff energy of 550 eV are used for the mechanical calculations. Symmetry-preserving deformations are applied in increments of 0.05% strain within the range of 1.5%, and the raw data are processed using the VASPKIT tool. The elastic constants are extracted by polynomial fitting of the stress-strain curves.

We determine the strength of the on-site Coulomb U and exchange J interactions between correlated electrons for magnetic systems within the cRPA method [23,24] as implemented in the SPEX code [25]. In this part, for the ground-state DFT calculations we use the FLEUR code [26], which is based on the full-potential linearized augmented plane-wave method. Here the calculations are performed using cutoff for the wave functions (k_{max}=4 a.u.$^{-1}$), and the $16 \times 16 \times 1$ k-point grid. The bands around the E_F, formed by TM d-orbitals in M_2X_2, are chosen as a target correlated subspace. The maximally localized Wannier functions are constructed using the WANNIER90 library [27]. We use a $9 \times 9 \times 1$ k-point grid for all structures in the cRPA calculations.

III. RESULTS AND DISCUSSION

A. Stability of M_2X_2 monolayers

Let us start by discussing the energetics and stability of M_2X_2 monolayers. Our calculations encompass a wide range of compounds, specifically M_2X_2 where M represents TM groups 3 to 11 elements and X represents S, Se, and Te. First, let us take a look at the formation energy E_f and the factors that influence it for M_2S_2 compounds. The unit cell of M_2S_2 consists of two M and two X atoms. The formation energies are determined using the equation $E_f = E_{tot}(M_2X_2) - 2E(M) - 2E(X)$, where $E_{tot}(M_2X_2)$ represents the total energy of 2D M_2X_2 per unit cell, and $E(M)$ and $E(X)$

denote the total energy of M and X per atom, respectively. The total energies of the M elements are derived from their most stable bulk structures. For X atoms (e.g., S, Se, and Te), E(X) is determined based on the total energies of their native elemental forms. For example, for sulfur it corresponds to orthorhombic α-sulfur which is the native and most stable form of sulfur under standard conditions. This approach allows for the calculation of formation energies by considering the total energies of the constituent atoms and the compound itself within the unit cell.

There are two dominant competing factors to the understanding of the formation energies of this class of compounds. The first factor involves the expansion of the TM lattice due to the insertion of chalcogen X atoms, and the second factor pertains to the hybridization between the valence d states on the TM and the p states of the chalcogen X. When the chalcogen X atoms are inserted into the TM lattice, the d band is narrowed, leading to a reduction in the d-band broadening contribution to the formation energy. The decrease in d-bond energy is closely related to the volume of the chalcogen X and the strength of the d bonding in the TM constituent. In Table I, we report the calculated formation energies E_f for the M_2S_2, M_2Se_2, and M_2Te_2 phases. In all compounds, the formation energies obey the relation E_f (M_2S_2) $< E_f$ (M_2Se_2) $< E_f$ (M_2Te_2), suggesting that the M_2S_2 phases are more likely to be achieved with greater purity in experimental settings. The atomic radius of chalcogen increases as one move from X = S to Te. Consequently, the necessary volume expansion energy to accommodate S atoms will be lower regardless of the type of TM atoms. In other words, if the TM atoms are pulled farther apart, then the d bandwidth decreases, leading to a reduction in the d-band broadening contribution to the stability of the lattice. This is the main reason for the lower formation energies of the M_2S_2 compounds.

Additionally, as one progresses across the row from Ti to Cu, interatomic distance in original TM structures initially reduces up to the Cr atom beyond which it remains nearly constant up to the Co atom and finally slightly increases to Zn. So, the required volume expansion energy to accommodate any of the X elements exhibits a similar behavior. This is the reason that among the considered M_2S_2, Ti possesses the smallest formation energy. 3d TM atoms have a smaller interatomic distance than 4d and 5d TM atoms. As a result, hosting X will give a weaker expansion effect in 3d-based M_2S_2 systems. This more or less agrees with our calculated formation energy when we move from 3d to 5d compounds. The exceptions such as Zr_2S_2 are related to the effect of p-d hybridization which acts as a competing effect. When a compound is formed from a TM atom and a X element with a valence p shell, the d states of the TM hybridize with the p states of X to create bonding and antibonding hybrid states. This hybridization leads to a effective term in the heat of formation for a few compounds.

By analyzing the phonon dispersion and checking for negative frequencies, we can assess the stability of materials and identify any potential dynamical instabilities. Twenty-seven compounds are expected to be stable based on the phonon calculations (see Fig. S1, Fig. S2, and Fig. S3 of the Supplemental Material [28]) whose electronic structures will be discussed later. The other compounds may be dynamically unstable since they exhibit imaginary phonon branches. Here we have presented the phonon spectra for selected materials, that is, M_2S_2 (M = Zr, Re, Tc) and Mn_2Se_2 in Fig. 2. The results reveal that almost all phonon frequencies are positive, indicating that these four systems are in their equilibrium state. Consequently, it is anticipated that under suitable conditions various M_2X_2 monolayers maybe realized.

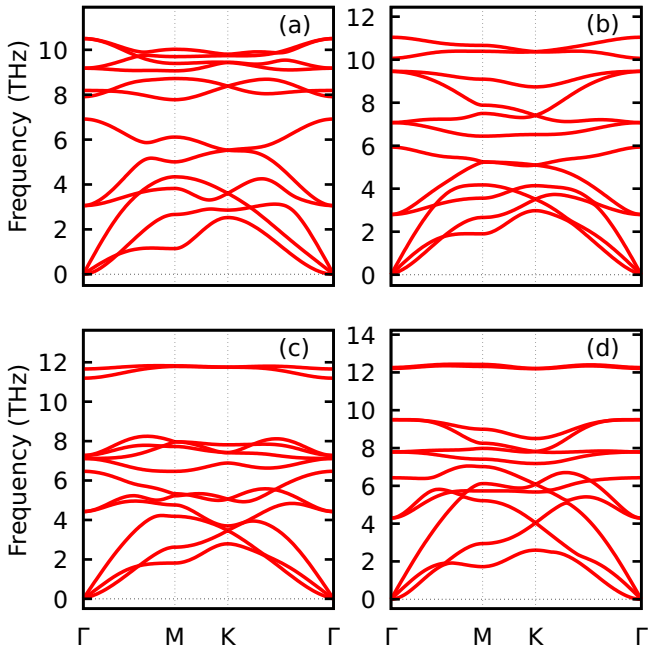


FIG. 2. Phonon dispersion of M_2S_2 monolayers (a) Zr_2S_2, (b) Mn_2Se_2, (c) Re_2S_2, and (d) Tc_2S_2.

Additionally, studying the thermal stability of a material is crucial for understanding energy fluctuations over time at various temperatures. The evolution of energy during the simulation and the final snapshots of the resulting geometries at 300 K of Tc_2S_2 and Zn_2S_2, illustrated in Figs. 3(a) and 3(b), respectively, is assessed through AIMD calculations. Both materials show no significant changes in their energy spectra, indicating that there are no broken bonds or geometric structure reconstructions after heating the system for 6500 fs. Time-dependent temperature fluctuation of Tc_2S_2 and Zn_2S_2 by AIMD simulations are also shown in Fig. 3. This observation confirms the thermodynamic stability of the M_2X_2 systems.

Beyond the demonstrated dynamical and thermal stability from phonon dispersion calculations, we thoroughly evaluate the thermodynamic stability of the predicted M_2X_2 monolayers relative to competing bulk phases. This was achieved by calculating the energy above the convex hull, ΔH_{hull}, which evaluates the phase's stability against decomposition into any combination of elemental solids or other stable compounds within the M-X binary system. The convex hull energy across all systems is presented in Fig. 4. It shows that significant number of the dynamically stable structures are found to be thermodynamically stable ($\Delta H_{\text{hull}} \approx 0$ meV/atom) or metastable with a very small positive energy ($\Delta H_{\text{hull}} < 0.1$ eV/atom), indicating a high potential for experimental synthesizability. Furthermore, as shown in inset of Fig. 4, a detailed

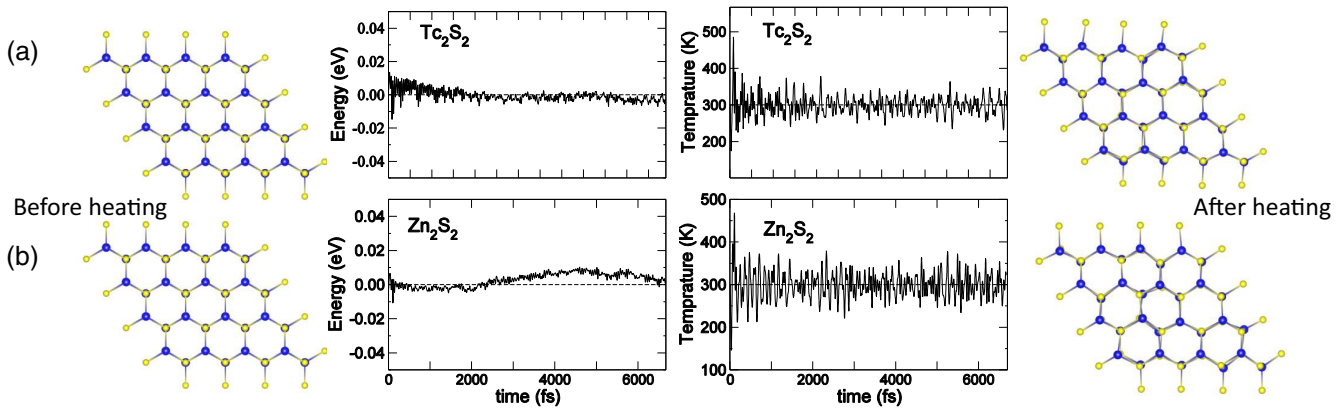


FIG. 3. [(a) and (b)] The evolution of energy during the simulation, time-dependent temperature fluctuation, and the final snapshots of the resulting geometries at 300 K of Tc_2S_2 and Zn_2S_2 through AIMD calculations.

analysis of the formation energy as a function of composition for representative systems, such as Zr_xS_{1-x} (see also Supplemental Material for Fe_xSe_{1-x} [28]), confirms that the M_2X_2 stoichiometry (at $x = 0.5$) lies on or in close proximity to the convex hull. This comprehensive thermodynamic investigation, coupled with their dynamical stability, strongly underpins the viability of these novel 2D materials.

B. Mechanical properties

Now we explore the mechanical characteristics of stable structures by examining elastic coefficients, in-plane stiffness Y_{2D}, shear modulus G, and Poisson's ratio ν. By analyzing the elastic strain tensors C_{ij}, we can derive the mechanical properties and assess elastic stability. The calculated values of C_{ij} are reported in Table II. For the 2D hexagonal systems we designed, elastic stability is confirmed when all C_{ij} values are positive and obey the Born and Huang criteria [29,30], which stipulate that $C_{11} > |C_{12}|$. Table II indicates that structures exhibiting dynamic stability also demonstrate mechanical stability. In the context of two dimensions, Y_{2D} quantifies the

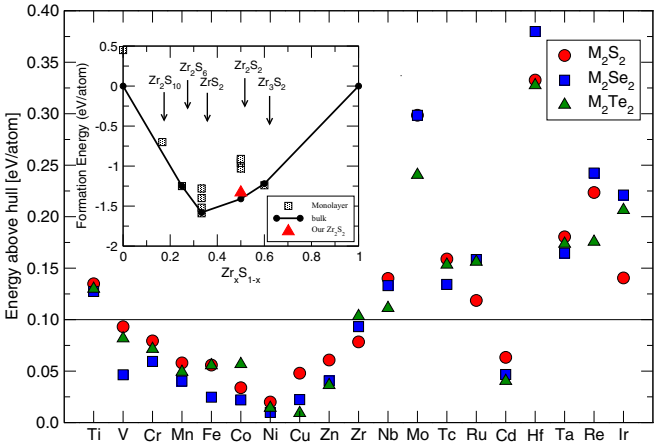


FIG. 4. The energy above hull for all M_2X_2 systems as a function of the transition metal M. Inset shows the formation energy as a function of composition x for Zr_xS_{1-x}, comparing the energy of our monolayer M_2X_2 phase to the convex hull constructed from all stable bulk reference phases.

TABLE II. Relaxed-ion elastic coefficients C_{ij}, 2D Young's modulus Y_{2D}, shear modulus G, and Poisson's ratio ν for stable M_2X_2 structures.

M_2X_2	$C_{11} = C_{22}$ (N m^{-1})	C_{12} (N m^{-1})	Y_{2D} (N m^{-1})	$G = (C_{11}\text{-}C_{12})/2$ (N m^{-1})	ν (−)
Ti_2S_2	110.9	49.6	88.8	30.7	0.45
Ti_2Se_2	90.8	42.1	71.3	24.4	0.46
V_2Se_2	100.8	53.7	72.2	23.6	0.53
V_2Te_2	83.3	44.9	59.1	19.2	0.54
Mn_2S_2	98.0	18.0	94.7	40.0	0.18
Mn_2Se_2	90.7	19.3	86.6	35.7	0.21
Fe_2S_2	148.6	53.0	129.7	47.8	0.36
Fe_2Se_2	102.9	27.6	95.5	37.6	0.27
Fe_2Te_2	105.1	53.8	77.6	25.7	0.51
Co_2S_2	138.4	52.8	118.3	42.8	0.38
Co_2Se_2	112.9	43.1	96.5	34.9	0.38
Co_2Te_2	98.0	33.0	86.9	32.5	0.34
Cu_2S_2	92.3	35.8	78.4	28.2	0.39
Cu_2Se_2	68.6	29.5	55.9	19.5	0.43
Cu_2Te_2	66.8	29.3	54.0	18.8	0.44
Zn_2S_2	98.2	27.7	90.4	35.2	0.28
Zn_2Se_2	79.1	23.2	72.3	27.9	0.29
Zn_2Te_2	66.4	19.2	60.8	23.6	0.29
Zr_2S_2	114.3	53.8	89.1	30.3	0.47
Zr_2Se_2	95.8	46.6	73.1	24.6	0.49
Nb_2Te_2	88.2	52.2	57.3	18.0	0.59
Tc_2S_2	126.5	66.9	91.2	29.8	0.53
Tc_2Se_2	132.2	51.3	112.3	40.4	0.39
Tc_2Te_2	102.6	53.0	75.2	24.8	0.52
Ru_2S_2	146.9	60.5	122.1	43.3	0.41
Ru_2Se_2	119.9	54.6	94.9	32.6	0.46
Ru_2Te_2	102.1	50.5	77.1	25.8	0.49
Cd_2S_2	79.6	25.1	71.7	27.2	0.32
Cd_2Se_2	65.9	21.7	58.8	22.1	0.33
Cd_2Te_2	54.3	17.3	48.9	18.5	0.32
Hf_2S_2	127.4	61.8	97.5	32.8	0.49
Ta_2Te_2	99.4	60.7	62.4	19.4	0.61
Re_2S_2	169.5	66.4	143.5	51.6	0.39
Re_2Se_2	148.3	59.9	124.1	44.2	0.40
Ir_2Se_2	127.3	57.6	101.5	34.9	0.45

rigidity or flexibility of a crystal when subjected to external loads, calculated using the formula: $Y_{2D} = (C_{11}^2 - C_{12}^2)/C_{11}$. The calculated Y_{2D} values for the monolayers of Zr_2S_2, V_2Se_2, Re_2S_2, and Tc_2S_2 are 89.1, 72.2, 143.5, and 91.2 N m^{-1}, respectively. Due to the symmetric and isotropic nature of the crystal structures analyzed, the Y_{2D} values in the x direction are equivalent to those in the y direction.

Comparison of Y_{2D} with other well-known 2D materials, namely graphene (341.1 N m^{-1}), $MoSi_2N_4$ (491.5 N m^{-1}), MoS_2 (124.5 N m^{-1}), and h-BN (275.9 N m^{-1}), reveals that M_2X_2 materials are mechanically as stable as MoS_2 but less stiffer than $MoSi_2N_4$ and single layer h-BN [31–33]. To elucidate the impact of applied stress on the mechanical properties of the systems, we determined the Poisson's ratio ν of the materials. The Poisson's ratio is defined as the negative ratio of transverse contraction strain to longitudinal extension strain in the direction of the stretching force. Utilizing the elastic tensor C_{ij}, ν is calculated using the formula $\nu = C_{11}/C_{12}$. The obtained results fall within the range of 0.29 to 0.54, as presented in Table II. For comparison, the reported values of ν for $MoSi_2N_4$ and MoS_2 crystals are 0.28 and 0.25, respectively [32,33].

C. Electronic and magnetic properties

In this section, we present the results of our investigation of the electronic and magnetic properties of each M_2S_2 systems. Electronic structures reveal that M_2S_2 can be classified into three distinct categories depending on TM atoms. These categories are referred to as metals, semiconductors or semimetals, and magnetic metals. The projected band structures depicted in Fig. 5 (see also Figs. S4 to S6 in supplementary material [28]) show that compared to the other orbitals from chalcogen atoms, the d orbitals of the TM atom significantly contributes to the bands near the Fermi level (with some exceptions). Thus, similarly to other stable TM-based materials such as TMDs and MXenes [7,9], all investigated M_2S_2 compounds can be described by an effective low-energy model based on only d electrons of TM atom. In most considered systems, the p bands of X atoms appear below the d bands of the TMs separated by a large energy difference.

1. Nonmagnetic metals

Our first-principles calculations indicate that the most stable M_2X_2 systems are metallic. Figure 5 shows projected band structure and densities of states of M_2S_2 compounds. Additionally, we reported electronic structure of all other M_2X_2 compounds in the supplementary material [28]. For instance, in the case of V_2S_2, the states around the E_F of these compounds are primarily dominated by the d orbitals of the V atoms, as shown in Fig. 5(b). The compounds exhibit common patterns of hybridization, with bonding states between the d orbitals of M and the p orbitals of X located below E_F. Above these bonding states, nonbonding states of M are located near the E_F. In V_2S_2, the p states of X atoms are partially hybridized with M d-orbitals below the E_F between –4.0 and –6 eV, and they are separated by a 2-eV band gap from the d bands of V. From Fig. 5(a) to Fig. 5(g), admixture of chalcogen p with d states increase as one moves from M = Ti to Cu-based systems. Indeed, as we move from Ti to Cu, the chalcogen p states gradually move to the higher energy and are accompanied by TM d bands. In Fig. 5, moving again from left Zr to right Ru for 4d TM in the periodic table (Hf to Tc for 5d TM), the same increasing trend is observed for X-p and M-d energy separation. S, Se, and Te have same valence electrons in their last electronic shells. Hence, the M_2Se_2, and M_2Te_2 compounds follow almost the same electronic structure as the M_2S_2 systems. Ongoing from S to Te within each M_2X_2 system, the lattice constant increases (see Table I), as a consequence, the longer bond lengths lead to larger dispersion for bands with X-p character. It can bring the states energetically closer together as shown in Fig. S6 of the supplementary material for the Te-based structure [28]. Such smaller energy difference in the M_2S_2-M_2Se_2-M_2Te_2 sequence has been observed in some other 2D TM materials such as TMDs and TM-halides [19,34].

2. Semimetals and semiconductors

While most of the M_2X_2 have metallic behavior, a few of them such as M_2X_2 (M = Zn, Cd) are direct band-gap semiconductors [Fig. 5(h) and Fig. 5(n)]. Since the simple GGA method is known to potentially underestimate band-gap values, the computationally more expensive HSE functionals are utilized to enhance the accuracy of band-gap estimation. We report the sizes of the band gaps of all the semiconducting monolayers in Table I based on both the standard DFT + PBE and HSE06 calculations. Some applications of these compounds include electronic devices, photonic and energy harvesting devices, novel spin qubit frameworks for quantum computation applications, and solar cells. The computed energy gap E_g varies in the range 0.9–2.6 eV (1.3–3.7 eV) at the DFT + PBE (HSE06) level. As seen in Table I, the E_g tends to reduce when X is varied from S to Te.

Figure 5(h) displays the corresponding projected electronic structure for the Zn_2S_2, which highlights the significant contribution of the 4p orbital of Zn and 3p orbital of S atoms to the valence band region near the E_F, while the 5s orbital of Zn dominates in the conduction band region. The semiconducting nature can be understood based on the structural properties and the electron filling of outer shell. Here, after bond formation, the 3d orbitals of Zn atoms are expected to be nearly full due to charge compensation of each atom which makes this system semiconducting.

In addition to these wide band-gap semiconductors, M_2X_2 (M = Ti, Zr, Hf) and M_2X_2 (M = Tc, Re) become semimetals in this family with more or less similar energy dispersion based on GGA + PBE method. This similar behavior among Ti, Zr, and Hf (same as Tc and Re) can be attributed to the fact that they belong to the same group in the periodic table and have the same number of electrons in their outermost atomic orbital shells. As a result, M_2X_2 systems derived from these elements demonstrate similar semimetallic behavior when placed in the same crystal structure. This semimetallic behavior (conelike shape) [35,36] has not been observed in other 2D materials such as TMDs, MXenes, TM halides, and intercalated architecture MA_2Z_4 and therefore remains an exclusive property of this family. Note that the top of valence band of M_2X_2 (M = Ti, Zr, Hf) compounds touch conduction

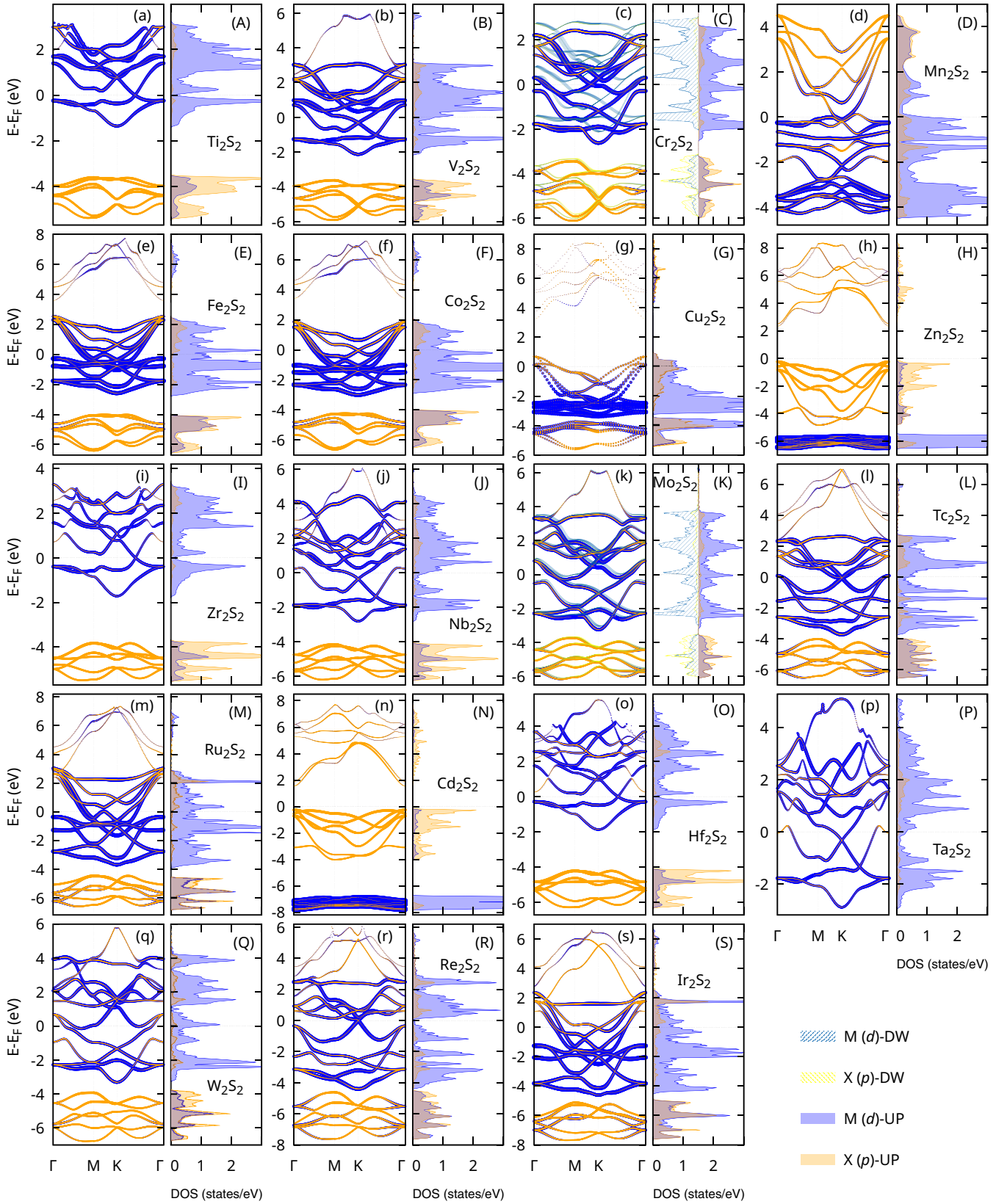


FIG. 5. Band structure and DOS projected onto *d* states of the M atom (blue color) as well as on *p* states of the X atoms (orange color) for M_2S_2 materials. For spin-polarized calculations, dark color (light color) correspond to spin-up (spin-down) states.

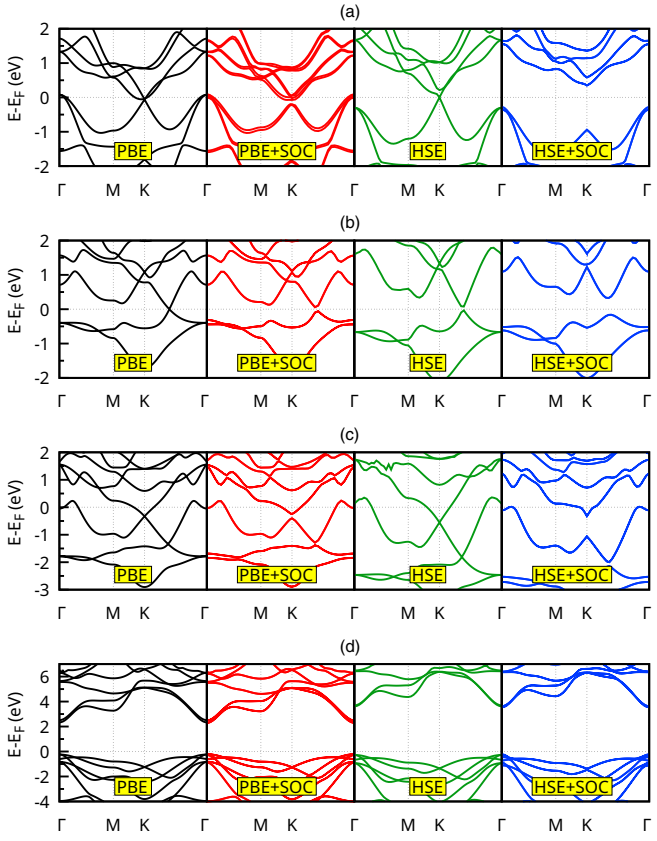


FIG. 6. PBE, PBE + SOC, HSE06, and SOC + HSE06 band structure of (a) Tc_2S_2, (b) Zr_2S_2, (c) Ta_2S_2, and (d) Zn_2S_2. The Fermi level is set to zero energy.

band at k point along KΓ path, while in the case of M_2X_2 (M = Tc, Re) the band crossing happens at high-symmetry K point. The electronic band structures of M_2S_2 (M = Zr, Tc, Ta, Zn) are calculated with consideration of the SOC, as depicted in Fig. 6. In all cases, a strikingly similar behavior is observed in the band structures calculated with and without SOC contributions. In the case of Zr_2S_2 and Tc_2S_2, it is noted that the conduction-band minimum (CBM) slightly shifts upwards, while the valence-band maximum (VBM) shifts downwards, resulting in a narrow band-gap opening of approximately 0.1 eV due to the presence of SOC making them potentially useful as infrared detectors or sensors. Our HSE calculations indicate that M_2X_2 (M = Ti, Zr; X = S, Se) are a direct band-gap semiconductor with E_g between 0.49 to 0.99 eV. The band dispersion and band-gap opening for compounds with conelike bands at high-symmetry K point (in the level of GGA + PBE) is different and more complicated. For example in the case of Tc_2S_2, system is still semimetal in HSE calculation. We found that in both PBE+SOC and HSE+SOC calculation, the band gap is indirect and is significantly larger than corresponding one for Zr_2S_2.

To further analyze the orbital character in band structure of semimetallic systems, we have investigated the projected band structure of the Zr_2S_2 and Tc_2S_2, as shown in Figs. 7(a)–7(e) and Figs. 7(f)–7(j), respectively. One can easily find that VBM and CBM for the Zr_2S_2 are formed by the d_{xz}/d_{yz} and $d_{xy}/d_{x^2-y^2}/d_{z^2}$ states of TM atoms, respectively. This confirms

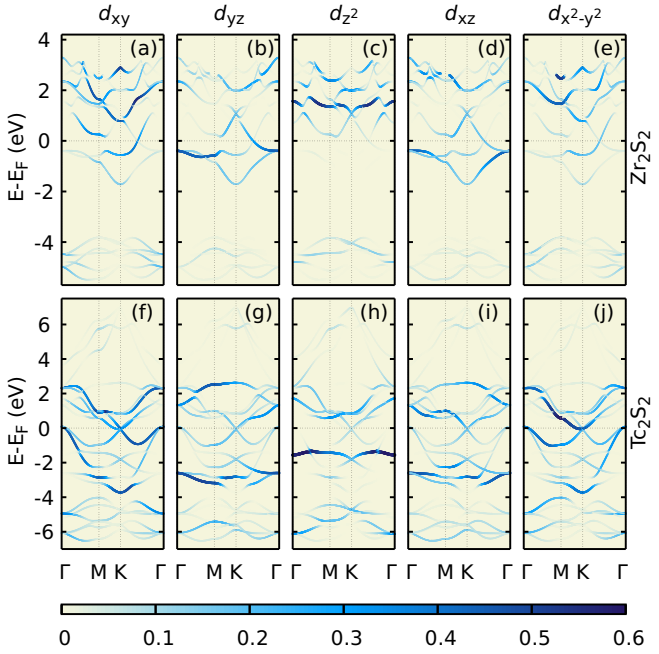


FIG. 7. The orbital-projected band structure for d electrons of TM atom of (a)–(e) Zr_2S_2 and (f)–(j) Tc_2S_2 based on DFT-PBE.

the symmetry discussion that d_{xz} and d_{yz} are farther from the ligands than the others and therefore experiences less repulsion. Note that the valence bands (conduction bands) are not of pure d_{xz}/d_{yz} ($d_{xy}/d_{x^2-y^2}/d_{z^2}$) character and the symmetry allows mixtures from from X-p states. This denominations thus refer to their dominant orbital character. In the case of Tc_2S_2, the d_{xz}/d_{yz} states are almost occupied and the bands with $d_{xy}/d_{x^2-y^2}$ character are dominant at the vicinity of E_F that participate in the formation of the Dirac cone.

Since the Dirac cone in Tc_2X_2 and Re_2X_2 occurs at the K point similarly to the well-known graphene, where relativisitc fermions aspects are combined with the strongly correlated aspects in the same system. Therefore they hold a great promise as a platform for correlated relativistic fermions allowing to explore combination of topological and many-body aspects. Let us list the two conceptual difference between Tc_2S_2 and graphene. First, the d states participate in the formation of the Dirac cone, whereas in graphene, the carbon p_z states play this role. Second, the two bands meeting at Fermi level and forming the Dirac cone in Tc_2S_2 are not isolated from other bands. As shown in Fig. 7(f) and Fig. 7(j), a quadratic band at E_F with $d_{xy}/d_{x^2-y^2}$ character coexists with two d_{xz}/d_{yz} bands. Therefore, we expect that applying biaxial pressure will couple with the $d_{xy}/d_{x^2-y^2}$ states and create significant band structure variation. This can serve as a convenient tool for the engineering of such a rich Dirac-Schrödinger bands. For these reasons, we examined the effect of strain on the electronic properties of Tc-based system. Figure 8 displays the band structure of Tc_2S_2 for different tensile strain. As seen, the quadratic band at the Fermi surface moves away from the Dirac bands with a moderate strain of about 5%, resulting in a clearly defined Dirac cone in the Tc_2S_2. This is a unique platform that allows to study the interplay between Dirac and quadratic bands where the coupling between the relativistic

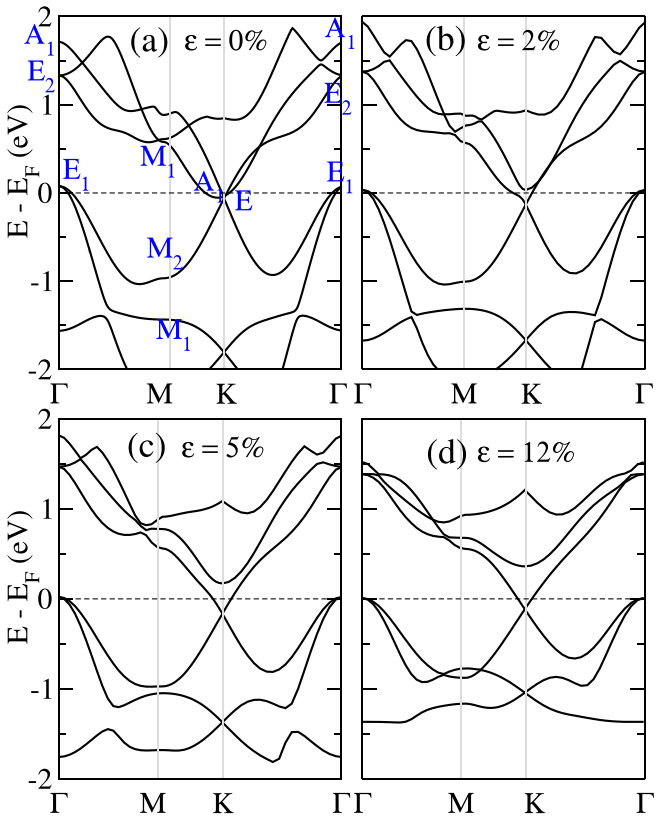


FIG. 8. The total band structure for Tc_2S_2 strained structures with (a) free state (not strain), (b) 2% tensile strain, (c) 5% tensile strain, and (d) 12% tensile strain based on DFT-PBE.

fermions in the Dirac bands and nonrelativistic fermions in the quadratic bands can be tuned by the external influence of the strain.

3. Magnetic metals

The number of 2D materials that naturally display magnetic ordering in their pristine form is quite limited. Among the vast number of 2D materials, only MX_3 (M = V, Cr; X = Br, I) [16,37,38], $Cr_2Ge_2Te_6$ [17], and MX_2 (M = V, Mn; X = Se, Te) [38–44] have been experimentally observed to exhibit magnetic orderings. Theoretical predictions have suggested the presence of intrinsic ferromagnetism in monolayers of M_2C MXenes like Ti_2X (X = C, N), Cr_2C, and V_2C [9,45–49], but this has not been experimentally confirmed. Even for most of the 3*d*-TMDCs like CrX_2 and MnX_2 systems, as well as VX_2, the origin of the intrinsic ferromagnetism remains controversial and the existence of a magnetic phase is still debated [39,50–53]. In other words, conflicting studies have suggested that the observed ferromagnetism in 3*d*-TMDCs is actually *extrinsic* 2D magnetism arising from vacancies [54] or proximity effects [55,56], which cannot be definitively ruled out in the growth of 2D crystals. The emergence of such extrinsic magnetic moments and long-range magnetic order induced by atomic vacancies or edge states in other 2D nonmagnetic materials like graphene [57–62] and MoS_2 [63,64] makes it more plausible that pristine TMDCs lack intrinsic 2D magnetism. The scarcity of magnetic materials

TABLE III. The energy difference between the total energy of ferromagnetic and nonmagnetic phases $E_m = E_{FM} - E_{NM}$, energy difference between the total energy of antiferromagnetic and ferromagnetic configurations $E_{ex} = E_{AFM} - E_{FM}$, the magnetic moment of TM atoms μ^{PBE} in the unit of μ_B, Density of state at Fermi level $D(E_F)$, effective Stoner parameter $I = (U + 6J)/5$, and exchange constant used in Heisenberg Hamiltonian J_H.

M_2X_2	E_m (meV)	E_{ex} (meV)	μ^{PBE} (μ_B)	$D(E_F)$ (1/eV)	I (eV)	J_H (meV)
Cr_2S_2	−59.5	40.1	1.3	0.72	1.47	11.9
Mn_2S_2	0.0	−297.4	2.3	0.47	1.51	−28.1
Mo_2S_2	−2.7	2.7	0.5	0.87	1.34	5.4
Cr_2Se_2	−8.8	−28.3	1.3	0.53	1.34	−8.4
Mn_2Se_2	0.0	−438.1	2.5	0.27	1.32	−35.1
Fe_2Se_2	−95.9	−102.1	2.7	0.61	1.38	−7.0
Mo_2Se_2	−1.2	1.2	0.3	0.83	1.24	9.6
Ti_2Te_2	−29.7	29.7	1.5	1.24	0.95	6.6
V_2Te_2	0.0	−6.5	0.7	0.49	1.20	−6.5
Cr_2Te_2	−1.1	−110.2	1.8	0.49	1.08	−18.0
Mn_2Te_2	−60.4	−396.9	2.5	0.21	1.09	−31.7
Fe_2Te_2	−334.0	284.4	4.5	1.06	1.18	7.2
Hf_2Te_2	−31.1	31.1	1.4	0.92	1.14	2.6

can be attributed to the robust covalent bonding between the TM and the X element. However, external strain can modify the covalent bonds, causing the release of *d* electrons and thereby giving rise to magnetism [65,66]. For instance, when tensile strain increases in M_2C MXenes, the magnetic moments are significantly boosted, leading to a transition from nonmagnetic states to ferromagnetic state in parent nonmagnetic MXenes [67,68]. The most notable transition is observed in Hf_2C, where the magnetic moment rises to 1.5 μ_B/unit at a strain of 1.8% [67]. Therefore finding new families of 2D materials possessing intrinsic magnetically nontrivial state is highly desirable.

In our M_2X_2 system, due to the the weak covalent bonding between the TM and the X element, we expect more of these materials to be magnetic in M_2X_2 family compared to other TM-based materials. To identify the preferable magnetic ordering in M_2X_2 systems, we set the spin ordering to either ferromagnetic (FM) or antiferromagnetic (AFM), as shown in Fig. S7. The exchange energy (E_{ex}) is calculated as $E_{ex} = E_{AFM} - E_{FM}$. Positive exchange energy indicates that the ground state of the system is ferromagnetic. Our calculations suggest that the ground states of Cr_2S_2, M_2Te_2 (M = Fe, Hf), and Ti_2Te_2 systems are ferromagnetic, while Mn_2X_2 (X = S, Se, Te), Cr_2X_2 (X = Se, Te), Fe_2Se_2, and V_2Te_2 are antiferromagnetic as shown in Table III. The nonpositive values of the first column that gives the energy difference $E_m = E_{FM} - E_{NM}$ indicates that nonmagnetic states is now the lowest-energy state. Then the second column decides whether the FM or AFM is the preferred state. As expected, the magnetic characteristics of these systems arise from the *d* orbitals of TM atoms. The magnetic moments of TM atoms in these systems are reported in Table III.

The value (also sign) of direct exchange and M–X–M superexchange can be controlled by the M–X–M bond angles as well as *d* electron configurations of TM atoms:

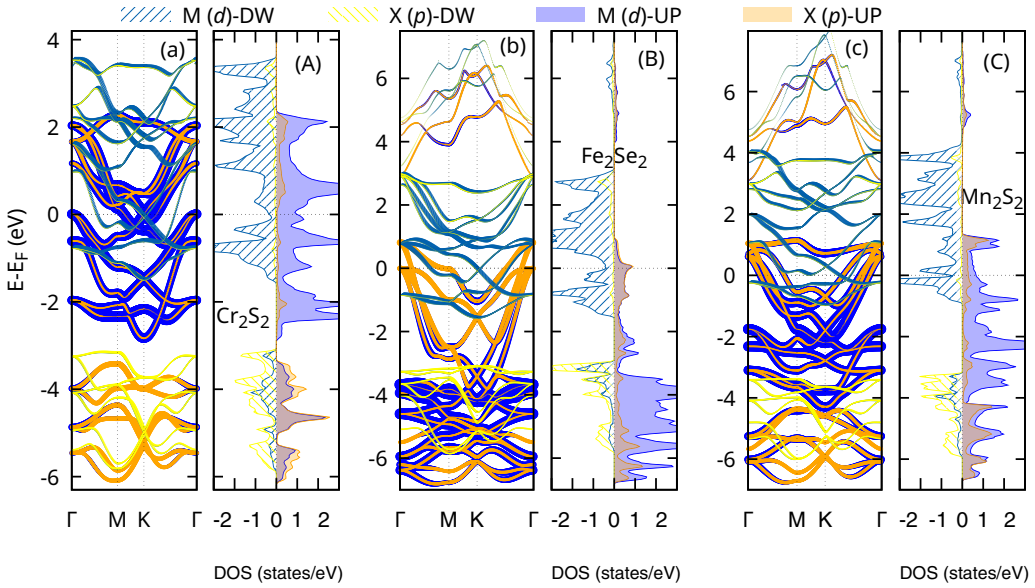


FIG. 9. The spin-polarized band structure and density of states for three representative correlated systems (a) Cr_2S_2, (b) Fe_2Se_2, and (c) Mn_2S_2 calculated with DFT + U.

According to the Goodenough-Kanamori-Anderson formalism, in systems with 90° bond angles the d-orbitals on neighboring TM atoms overlap with different halogen-p orbitals and the superexchange interaction between TM atoms is always FM [69–71]. In M_2X_2 compounds, all calculated metal-halogen-metal bond angles are between 60° and 65°. In such a case, d orbitals on neighboring TM atoms are not able to completely overlap with two orthogonal chalcogen-p orbitals. So FM superexchange is weakened due to deviation of the M–X–M bond angles from 90°. On the other hand, the presence of 60° M–X–M bond angles causes the TM atoms to come closer to each other and enhance the AFM direct exchange interaction. That is why most of the magnetic M_2X_2 materials are in the AFM phase.

As most of the M_2X_2 systems contain partially filled d TM atoms in nonmagnetic calculation, we can use the simple Stoner model to discuss the appearance of ferromagnetism in these materials. Based on this model, the instability of the paramagnetic state towards ferromagnetic ordering is given by the criterion $I.D(E_F) > 1$, where I is the Stoner parameter and $D(E_F)$ is the DOS at the E_F in the nonmagnetic state at the Fermi level. Within the multiorbital Hubbard model, the relationship between the Stoner parameter I, Hubbard U, and exchange J is given by $I = (U + 6J)/5$ [72]. On the basis of the calculated effective Coulomb parameters U and J determined by first principles using the cRPA method, $I.D(E_F)$ values for ferromagnetic compounds are put together in Table III.

For most of the FM M_2X_2, we observe substantial $D(E_F)$ values and subsequently large $I.D(E_F)$ values, exceeding those found in NM and AFM M_2X_2 materials. Consequently, the significant DOS of Ti, Cr, Fe, Mo, and Hf atoms at the E_F in Ti_2Te_2, Cr_2S_2, Fe_2Te_2, Mo_2X_2 (X = S, Se), and Hf_2Te_2, respectively, can lead to instability in magnetic ordering, which agrees well with our findings from spin-polarized total energy calculations and the substantial computed magnetic moments. The spin-polarized density functional calculations indicate that the ground states of the V_2X_2, Co_2X_2, and Cu_2X_2 are nonmagnetic because of the small $D(E_F)$.

Standard DFT approach can be insufficient for strongly correlated d transition metals. So we perform additional DFT + U calculations for selected magnetic systems, using the calculated Hubbard U and J parameters derived from cRPA for each specific transition metal atom in its coordination environment. To explicitly discuss this, we depicte the electronic band structure and density of states for three representative correlated systems Cr_2S_2, Fe_2Se_2, and Mn_2S_2 calculated with GGA + U in Fig. 9. The inclusion of a U correction enhances the spin-splitting and leads to an increase in the local magnetic moments on the 3d metal atoms. The magnetic moment of TM atoms in Cr_2S_2, Mn_2S_2, and Fe_2Se_2 reaches values of 1.6 μ_B, 2.9 μ_B, and 3.4 μ_B respectively. Crucially, while the quantitative values of the magnetic moments are improved, the overall magnetic ground state ordering (e.g., ferromagnetic vs antiferromagnetic) reported in our original manuscript remain robust and the magnetic-metallicity of the compounds does not transform into a half-metallic or magnetic-semiconducting state.

Finally, we derive the magnetic exchange constant J_H for the nearest-neighboring M atoms using the total energies obtained from DFT calculations. The exchange constant J_H is derived from the exchange energy as follows:

$$J_H = \frac{E_{\mathrm{AFM}} - E_{\mathrm{FM}}}{2zS_{\mathrm{TM}}^2}, \tag{2}$$

where E_{AFM} and E_{FM} are total energy per TM atom for antiferromagnetic and ferromagnetic states, respectively, z is the number of nearest TM neighbors. Here $z = 4$ for single-layer M_2X_2. S_{TM} is the magnetic moment of each TM atom. Our calculated exchange constants for magnetic systems are summarized in Table III. These values of J_H can be employed

in model Hamiltonian calculations to estimate the critical properties of ferromagnetic materials such as Curie temperature T_C.

IV. CONCLUSION

Employing DFT calculations, we have predicted a novel family of 2D compounds built around TM under the classification M_2X_2 (with M symbolizing TM and X representing chalcogen elements like S, Se, and Te). These materials can be viewed as a AB stacking of two honeycomb MX layers. Each MX layer shares a similar structure to graphene but consists of alternating M (sublattice A) and X (sublattice B) atoms arranged in a buckled hexagonal lattice. Our study encompasses a thorough exploration into the formation energies, dynamical or thermal stabilities, mechanical properties, electronic structures, and magnetic properties of different systems within this compound family. Our computational analyses have unearthed 35 thermodynamically and dynamically stable M_2X_2 monolayer materials that exhibit remarkable diversity in their electronic and magnetic attributes. These findings are poised to pave the way for the experimental realization of a range of M_2X_2 structures with elusive and useful properties. Specifically, within the assortment of projected compounds, M_2X_2 (where M = Zn, Cd and X = S, Se, Te) emerge as direct band-gap semiconductors, exhibiting E_g ranging from 1.3 to 3.7 eV through hybrid functional calculations. A higher degree of control over the valleys in this new family of semiconductors is also promising for a new generation of semiconductor based spin qubits. Possibility of employing strain gauge fields similar to those in graphene nail down the valley degree of freedom in this new 2D semiconductors rises hopes for valley nondegenerate spin qubits in this systems. On the other hand, the compounds M_2X_2 (M = Ti, Zr, Hf, Tc, Re) behave as zero-gap semiconductors or semimetals when analyzed using standard DFT + PBE calculations. However, the inclusion of spin–orbit coupling opens a band gap of approximately 0.1 eV in these materials. This broad range of band gaps suggests a diverse potential for applications in optoelectronic devices, particularly in areas requiring *tunable* electronic properties. Interestingly, our examination has revealed *intrinsic* magnetic properties in the present class of materials, such as Mn_2X_2 (X = S, Se), Fe_2X_2 (X = Se, Te), and Ti_2Se_2. The identification of intrinsic magnetism in M_2X_2 materials not only provides valuable insights into the magnetic behavior of 2D systems but also positions these substances as promising candidates for the advancement of cutting-edge spintronics devices.

ACKNOWLEDGMENT

S.A.J. was supported by Alexander von Humboldt foundation and EinQuantumNRW.

DATA AVAILABILITY

The data supporting this study's findings are available within the article.

[1] E. C. Ahn, npj 2D Mater. Appl. **4**, 17 (2020).
[2] H. Li, J. Wu, Z. Yin, and H. Zhang, Acc. Chem. Res. **47**, 1067 (2014).
[3] A. Avsar, H. Ochoa, F. Guinea, B. Ozyilmaz, B. J. van Wees, and I. J. Vera-Marun, Rev. Mod. Phys. **92**, 021003 (2020).
[4] S. H. Suk, S. B. Seo, Y. S. Cho, J. Wang, and S. Sim, Nanophoton. **13**, 107 (2024).
[5] H. Chen, J. Zhang, D. Kan, J. He, M. Song, J. Pang, S. Wei, and K. Chen, Crystals **12**, 1381 (2022).
[6] S. Manzeli, D. Ovchinnikov, D. Pasquier, O. V. Yazyev, and A. Kis, Nat. Rev. Mater. **2**, 17033 (2017).
[7] H. R. Ramezani, E. Sasioglu, H. Hadipour, H. R. Soleimani, C. Friedrich, S. Blugel, and I. Mertig, Phys. Rev. B **109**, 125108 (2024).
[8] Y. Gogotsi and B. Anasori, ACS Nano **13**, 8491 (2019).
[9] H. Hadipour and Y. Yekta, Phys. Rev. B **100**, 195118 (2019).
[10] B. Huang, G. Clark, E. Navarro-Moratalla, D. R. Klein, R. Cheng, K. L. Seyler, D. Zhong, E. Schmidgall, M. A. McGuire, D. H. Cobden, W. Yao, D. Xiao, P. Jarillo-Herrero, and X. Xu, Nature (London) **546**, 270 (2017).
[11] Y.-L. Hong, Z. Liu, L. Wang, T. Zhou, W. Ma, C. Xu, S. Feng, L. Chen, M.-L. Chen, D.-M. Sun, X.-Q. Chen, H.-M. Cheng, and W. Ren, Science **369**, 670 (2020).
[12] L. Wang, Y. Shi, M. Liu *et al.*, Nat. Commun. **12**, 2361 (2021).
[13] Y. Yin, Q. Gong, M. Yi, and W. Guo, Adv. Funct. Mater. **33**, 2214050 (2023).
[14] J. P. Perdew, K. Burke, and M. Ernzerhof, Phys. Rev. Lett. **77**, 3865 (1996).
[15] J. Heyd, G. E. Scuseria, and M. J. Ernzerhof, J. Chem. Phys. **118**, 8207 (2003).
[16] K. L. Seyler, D. Zhong, D. R. Klein, Sh Gao, X. Zhang, B. Huang, E. Navarro-Moratalla, L. Yang, D. H. Cobden, M. A. McGuire, W. Yao, D. Xiao, P. Jarillo-Herrero, and X. Xu, Nat. Phys. **14**, 277 (2018).
[17] Ch Gong, L. Li, Zh Li, H. Ji, A. Stern, Y. Xia, T. Cao, W. Z. Q. Qiu, R. J. Cava, S. G. Louie, J. Xia, and X. Zhang, Nature (London) **546**, 265 (2017).
[18] M. Bonilla, S. Kolekar, Y. Ma, H. C. Diaz, V. Kalappattil, R. Das, T. Eggers, H. R. Gutierrez, M. H. Phan, and M. Batzill, Nat. Nanotechnol. **13**, 289 (2018).
[19] A. K. Aghaee, S. Belbasi, and H. Hadipour, Phys. Rev. B **105**, 115115 (2022).
[20] P. E. Blochl, Phys. Rev. B **50**, 17953 (1994).
[21] G. Kresse and J. Furthmuller, Comput. Mater. Sci. **6**, 15 (1996); Phys. Rev. B **54**, 11169 (1996).
[22] A. V. Krukau, O. A. Vydrov, A. F. Izmaylov, and G. E. Scuseria, J. Chem. Phys. **125**, 224106 (2006).
[23] F. Aryasetiawan, M. Imada, A. Georges, G. Kotliar, S. Biermann, and A. I. Lichtenstein, Phys. Rev. B **70**, 195104 (2004); F. Aryasetiawan, K. Karlsson, O. Jepsen, and U. Schonberger, *ibid.* **74**, 125106 (2006); T. Miyake, F. Aryasetiawan, and M. Imada, *ibid.* **80**, 155134 (2009).

[24] Y. Nomura, M. Kaltak, K. Nakamura, C. Taranto, S. Sakai, A. Toschi, R. Arita, K. Held, G. Kresse, and M. Imada, Phys. Rev. B **86**, 085117 (2012); B.-C. Shih, Y. Zhang, W. Zhang, and P. Zhang, **85**, 045132 (2012).

[25] A. Schindlmayr, C. Friedrich, E. Sasioglu, and S. Blügel, in *Modern and Universal First-Principles Methods for Many-Electron Systems in Chemistry and Physics*, edited by F. M. Dolg (Oldenbourg, München, 2010), pp. 67–78.

[26] http://www.flapw.de/.

[27] G. Pizzi*et al.*, J. Phys.: Condens. Matter **32**, 165902 (2020).

[28] See Supplemental Material at http://link.aps.org/supplemental/10.1103/c2qq-vc5f for phonon dispersion, the projected band structure, and the corresponding projected density of states for all predicted materials.

[29] M. Born M and K. Huang, *Dynamical Theory of Crystal Lattices* (Clarendon, Oxford, 1954).

[30] F. Mouhat and F-X Coudert, Phys. Rev. B **90**, 224104 (2014).

[31] H. Sahin, S. Cahangirov, M. Topsakal, E. Bekaroglu, E. Akturk, R. T. Senger, and S. Ciraci, Phys. Rev. B **80**, 155453 (2009).

[32] D. Cakir, F. M. Peeters, and C. Sevik, Appl. Phys. Lett. **104**, 203110 (2014).

[33] A. Bafekry, M. Faraji, D. Hoat, M. Shahrokhi, M. Fadlallah, F. Shojaei, S. Feghhi, M. Ghergherehchi, and D. Gogova, J. Phys. D: Appl. Phys. **54**, 155303 (2021).

[34] Y. Yekta, H. Hadipour, E. Sasioglu, C. Friedrich, S. A. Jafari, S. Blugel, and I. Mertig, Phys. Rev. Mater. **5**, 034001 (2021).

[35] J. Wang, S. Deng, Z. Liu, and Z. Liu, Natl. Sci. Rev. **2**, 22 (2015).

[36] Y. Yekta, H. Hadipour, and S. A. Jafari, Commun. Phys. **6**, 46 (2023).

[37] M. C. D. Siena, S. E. Creutz, A. Regan, P. Malinowski, Q. Jiang, K. T. Kluherz, G. Zhu, Z. Lin, J. J. D. Yoreo, X. Xu, J. H. Chu, and D. R. Gamelin, Nano Lett. **20**, 2100 (2020).

[38] T. Kong, K. Stolze, E. I. Timmons, J. Tao, D. Ni, S. Guo, Z. Yang, R. Prozorov, and R. J. Cava, Adv. Mater. **31**, 1808074 (2019).

[39] G. Duvjir, B. K. Choi, I. Jang, S. Ulstrup, S. Kang, T. T. Ly, S. Kim, Y. H. Choi, C. Jozwiak, A. Bostwick, E. Rotenberg, J.-G. Park, R. Sankar, K.-S. Kim, J. Kim, and Y. J. Chang, Nano Lett. **18**, 5432 (2018).

[40] X. Wang, D. Li, Z. Li, C. Wu, C.-M. Che, G. Chen, and X. Cui, ACS Nano **15**, 16236 (2021).

[41] K. Lasek, P. M. Coelho, K. Zberecki, Y. Xin, S. K. Kolekar, J. Li, and M. Batzill, ACS Nano **14**, 8473 (2020).

[42] A. Purbawati, J. Coraux, J. Vogel, A. Hadj-Azzem, N. Wu, N. Bendiab, D. Jegouso, J. Renard, L. Marty, V. Bouchiat, A. Sulpice, L. Aballe, M. Foerster, F. Genuzio, A. Locatelli, T. O. Mentes, Z. V. Han, X. Sun, M. Nunez-Regueiro, and N. Rougemaille, ACS Appl. Mater. Interf. **12**, 30702 (2020).

[43] B. Li, Z. Wan, C. Wang, P. Chen, B. Huang, X. Cheng, Q. Qian, J. Li, Z. Zhang, G. Sun, B. Zhao, H. Ma, R. Wu, Z. Wei, Y. Liu, L. Liao, Y. Ye, Y. Huang, X. Xu, X. Duan, W. Ji, and X. Duan, Nat. Mater. **20**, 818 (2021).

[44] L. Meng, Z. Zhou, M. Xu, S. Yang, K. Si, L. Liu, X. Wang, H. Jiang, B. Li, P. Qin, P. Zhang, J. Wang, Z. Liu, P. Tang, Y. Ye, W. Zhou, L. Bao, H.-J. Gao, and Y. Gong, Nat. Commun. **12**, 809 (2021).

[45] T. Amrillah, A. Hermawan, Y. B. Cristian, A. Oktafiani, D. M. M. Dewi, I. Amalina, Darminto, and J.-Y. Juang, Phys. Chem. Chem. Phys. **25**, 18584 (2023).

[46] Y. Yue, J. Magn. Magn. Mater. **434**, 164 (2017).

[47] H. Tan, C. Wang, H. Duan, J. Tian, Q. Ji, Y. Lu, F. Hu, W. Hu, G. Li, N. Li, Y. Wang, W. Chu, Z. Sun, and W. Yan, ACS Appl. Mater. Interf. **13**, 33363 (2021).

[48] B. Akgenc, A. Mogulkoc, and E. Durgun, J. Appl. Phys. **127**, 084302 (2020).

[49] M. Khazaei, M. Arai, T. Sasaki, C.-Y. Chung, N. S. Venkataramanan, M. Estili, Y. Sakka, and Y. Kawazoe, Adv. Funct. Mater. **23**, 2185 (2013).

[50] J. Feng, D. Biswas, A. Rajan, M. D. Watson, F. Mazzola, O. J. Clark, K. Underwood, I. Markovi, M. McLaren, A. Hunter, D. M. Burn, L. B. Duffy, S. Barua, G. Balakrishnan, F. Bertran, P. L. Fèvre, T. K. Kim, G. van der Laan, T. Hesjedal, and P. D. C. King, Nano Lett. **18**, 4493 (2018).

[51] P. Chen, W. W. Pai, Y.-H. Chan, V. Madhavan, M. Y. Chou, S.-K. Mo, A.-V. Fedorov, and T.-C. Chiang, Phys. Rev. Lett. **121**, 196402 (2018).

[52] A. O. Fumega, M. Gobbi, P. Dreher, W. Wan, C. Gonzalez-Orellana, M. Pena-Diaz, C. Rogero, J. Herrero-Martin, P. Gargiani, M. Ilyn, M. M. Ugeda, V. Pardo, and S. Blanco-Canosa, J. Phys. Chem. C **123**, 27802 (2019).

[53] P. K. J. Wong, W. Zhang, F. Bussolotti, X. Yin, T. S. Herng, L. Zhang, Y. L. Huang, G. Vinai, S. Krishnamurthi, D. W. J. A. M. Bukhvalov, Y. J. Zheng, R. Chua, A. T. N'Diaye, S. A. Morton, C.-Y. Yang, K.-H. O. Yang, P. Torelli, W. Chen, K. E. J. Goh, J. Ding, A. H. C. Neto, and A. T. S. Wee, Adv. Mater. **31**, 1901185 (2019).

[54] R. Chua, J. Yang, X. He, X. Yu, W. Yu, F. Bussolotti, P. K. J. Wong, K. P. Loh, M. B. H. Breese, K. E. J. Goh, Y. L. Huang, and A. T. S. Wee, Adv. Mater. **32**, 2000693 (2020).

[55] G. Vinai, C. Bigi, A. Rajan, M. D. Watson, T.-L. Lee, F. Mazzola, S. Modesti, S. Barua, M. Ciomaga Hatnean, G. Balakrishnan, P. D. C. King, P. Torelli, G. Rossi, and G. Panaccione, Phys. Rev. B **101**, 035404 (2020).

[56] W. Zhang, L. Zhang, P. K. J. Wong, J. Yuan, G. Vinai, P. Torelli, G. van der Laan, Y. P. Feng, and A. T. S. Wee, ACS Nano **13**, 8997 (2019).

[57] O. V. Yazyev and L. Helm, Phys. Rev. B **75**, 125408 (2007).

[58] H. Hadipour, Phys. Rev. B **99**, 075102 (2019); H. Hadipour, E. Sasioglu, F. Bagherpour, C. Friedrich, S. Blugel, and I. Mertig, *ibid.* **98**, 205123 (2018).

[59] E. Sasioglu, H. Hadipour, C. Friedrich, S. Blugel, and I. Mertig, Phys. Rev. B **95**, 060408(R) (2017).

[60] M. M. Ugeda, I. Brihuega, F. Guinea, and J. M. Gomez-Rodriguez, Phys. Rev. Lett. **104**, 096804 (2010).

[61] F. Bagherpour, S. Mahdavifar, E. H. Lapasar, and H. Hadipour, Phys. Rev. B **109**, 165115 (2024).

[62] A. Montaghemi, H. Hadipour, F. Bagherpour, A. Yazdani, and S. Mahdavifar, Phys. Rev. B **101**, 075427 (2020).

[63] Z. Zhang, X. Zou, V. H. Crespi, and B. I. Yakobson, ACS Nano **7**, 10475 (2013).

[64] L. Cai, J. He, Q. Liu, T. Yao, L. Chen, W. Yan, F. Hu, Y. Jiang, Y. Zhao, T. Hu, Z. Sun, and S. Wei, J. Am. Chem. Soc. **137**, 2622 (2015).

[65] W. S. Yun, S. W. Han, S. C. Hong, I. G. Kim, and J. D. Lee, Phys. Rev. B **85**, 033305 (2012).

[66] Y. Zhou, Z. Wang, P. Yang, X. Zu, L. Yang, X. Sun, and F. Gao, ACS Nano **6**, 9727 (2012).

[67] S. Zhao, W. Kang, and J. Xue, Appl. Phys. Lett. **104**, 133106 (2014).
[68] J. A. Warner, S. K. R. Patil, S. V. Khare, and K. C. Masiulaniec, Appl. Phys. Lett. **88**, 101911 (2006).
[69] J. B. Goodenough, Phys. Rev. **100**, 564 (1955).
[70] J. Kanamori, J. Appl. Phys. **31**, S14 (1960).
[71] V. V. Kulish and W. Huang, J. Mater. Chem. C **5**, 8734 (2017).
[72] G. Stollhoff, A. M. Oles, and V. Heine, Phys. Rev. B **41**, 7028 (1990).